Volume 1 | Number 1 | Jan 2013 | Pages 1–100

Journal of
Materials Chemistry B

Materials for biology and medicine
www.rsc.org/materialsB

ROYAL SOCIETY
OF CHEMISTRY

ROYAL SOCIETY
OF CHEMISTRY

www.rsc.org/materialsB

Journal Name

Journal of Materials Chemistry B

ARTICLE TYPE

Hybrid Nanostructured Hydroxyapatite/Chitosan Composite Scaffold: Bioinspired Fabrication, Mechanical Property and Biological Property

Ya-Ping Guo,[a]† Jun-Jie Guan,[b]† Jun Yang[a], Yang Wang[b], Chang-Qing Zhang,[b]* Qin-Fei Ke[a]*

The fabrication of bone scaffolds with interconnected porous structure, adequate mechanical properties, excellent biocompatibility and osteoinductivity is still remained a great challenge. Herein, hybrid nanostructured hydroxyapatite/chitosan (HA/CS) composite scaffold has been fabricated according to following steps: (i) deposition of brushite/CS on CS fibre porous scaffold by dip-coating method; and (ii)
10 formation of hybrid nanostructured HA/CS composite scaffold by the *in situ* conversion of brushite to HA using a bioinspired mineralization process. The hybrid HA/CS composite scaffold possesses three-dimensional (3D) interconnected pores with a pore size of 30-80 μm. The HA rods with a length of ~200 nm and width of ~50 nm are perpendicularly oriented to the CS fibres. Interestingly, the above HA rods are composed of many smaller nanorods with a length of~40 nm and width of~10 nm along *c*-axis
15 orientation. Hybrid nanostructured HA/CS composite scaffold exhibits good mechanical properties with compression strength of 9.41 ± 1.63 MPa and elastic modulus of 0.17 ± 0.02 GPa, which are well-matched to those of trabecular bone. The influences of the hybrid HA/CS composite scaffold on cells have been investigated by using human bone marrow stem cells (hBMSCs) as cell model and the CS fibre porous scaffold as control sample. The hybrid HA/CS composite scaffold not only supports the adhesion
20 and proliferation of hBMSCs, but also improve the osteoinductivity. The alkaline phosphatase activity and mineralization deposition on the hybrid HA/CS composite scaffold are higher than those on the CS fibre porous scaffold. Moreover, the hybrid HA/CS composite scaffold can promote the formation of new bone in rat calvarial defects as compared with the CS fibre porous scaffold. The excellent biocompatibility, osteoinductivity and mechanical properties suggest that the hybrid nanostructured
25 HA/CS composite scaffold has great potential for bone tissue engineering.

1. Introduction

The repair of large bone defects resulting from trauma, traffic accidents and surgical resection remains an urgent and complicated problem in orthopedic surgery.[1,2] Autologous bone
30 grafts as the gold standard are used for repairing massive bone defects; however, the method requires another invasive surgery, and may cause infection, nerve damage and hemorrhage.[3,4] Fortunately, bone tissue engineering is a rapidly developing discipline, which provides a new strategy to repair, replace or
35 regenerate injured bone tissue. Ideal bone scaffolds for bone tissue engineering should have interconnected porous structure, adequate mechanical properties, excellent biocompatibility and osteoinductivity.[5,6]

The biological and mechanical properties of scaffolds depend
40 mainly on their chemical composition, crystallinity, crystallographic texture and microstructure. Research findings on natural bone provide an bioinspired way to design and prepare artificial bone scaffolds.[7,8] Natural bone is a hierarchically structured inorganic-organic composite material, consisting of
45 around 65 wt.% apatite mineral, 25wt.% organic (mostly type I

collagen) and 10 wt.% water.[9,10] Biological apatite nanocrystals with a low crystallinity are oriented and aligned within self-assembled collagen fibres.[9] In vertebrate bones and tooth enamel surfaces, the apatite crystals exhibit *c*-axis orientation and *a*(*b*)-
50 axis orientation, respectively.[11]

The hybrid nanostructured composites with the preferred orientation of apatite crystals along collagen fibres are believed to affect the biomechanical and biological performances of bone tissue. The high stiffness and strength of bones are attributed to
55 stiff apatite crystals, and the high fracture toughness is ascribed to ductile collagen.[12] Besides the mass faction of mineral (or organic matrix) in bones, the apatite crystal orientation has great effect on mechanical properties.[13,14] Inside each individual trabecular bone, the apatite *c*-axis preferentially aligns along the direction of the
60 trabecula, which makes the trabecula mechanically anisotropic.[15,16] Moreover, the biological properties of scaffolds are related to the crystallographic texture of HA crystals. The preferential *c*-axis orientation of HA crystals is a strong determinant and predictor of the mechanical function of tissue-
65 engineered bone.[17] The HA crystals with the surfaces exhibiting a tailored crystallographic texture enable a new level of control of cellular behaviour and enhance mineralized tissue formation.[18-20]

Scaffold materials for bone engineering tissue should not only have the similar chemical composition, crystallinity and crystallographic texture to natural bones, but also possess interconnected porous structure.[21] The three-dimensional (3D) interconnected macropores and appropriate porosities in bone scaffolds allow the ingrowth of bone tissue to achieve full integration with the living bones, and enable the transport of nutrients, oxygen and growth factors to the centre of the regenerated tissue.[22] In addition, a wide pore size distribution can create favorable local conditions that lead to the nucleation and growth of carbonate apatite.[23] Unfortunately, the interconnected macropores and high porosity may seriously weaken the mechanical strengths of porous scaffolds. Up to now, it still remains a challenge to prepare interconnected porous HA/polymer scaffolds with good mechanical properties well-matched to natural bones.

Recently, different kinds of synthesis strategies including electrospinning, thermally induced phase separation and freeze-drying process have been developed to fabricate HA/polymer composite scaffolds.[24-28] However, the morphology, crystallinity and crystallographic texture of the HA crystals in composite scaffolds are different from the minerals of natural bones. During the biomineralization process of bone minerals, an amorphous calcium phosphate (ACP) is converted to apatite crystals by using metastable crystalline phases such as octacalcium phosphate (OCP, $Ca_8H_2(PO_4)_6 \cdot 5H_2O$) and brushite (DCPD, $CaHPO_4 \cdot 2H_2O$) as transitory precursors, resulting in the formation of hybrid nanostructured collagen/apatite composites.[9] Herein, we mimicked the biomineralization process of the apatite in bone tissue to fabricate hybrid nanostructured HA/CS composite scaffold with HA nanorods perpendicularly oriented to CS fibres. The preparation process included the following stages: (i) deposition of DCPD/CS on CS fibre porous scaffold by dip-coating method; and (ii) formation of hybrid nanostructured HA/CS composite scaffold from the DCPD/CS composite scaffold by alkaline solution treatment. The main aims of this work were to fabricate hybrid nanostructured HA/CS composite scaffold with HA nanorods perpendicularly oriented to CS fibres, and to study their biocompatibility, osteoinductivity and mechanical properties.

2. Experimental

2.1 Preparation of CS fibre porous scaffold

The CS fibre porous scaffold was produced by a needle-punching process.[29] Briefly, the CS staple fibres (deacetylation degree: 85%, M_η: 4×10^5) were carded by using a laboratory carding machine (ASI8IA, Jiangxi textile equipment Co., Ltd, China) to form a fibrous web. Eight layers of the carded fibrous webs were arranged along the machine direction and then needled using a needle machine (F22G-I1600, Changshu Weicheng Non-Woven Equipment Co., Ltd, China) equipped with 4500 needles ($15 \times 18 \times 32 \times 3$, R333 G3027, Groz-Beckert, Albstadt, Germany) per running meter. The working frequency was 690 needles per minute, and the needle rate was 3.63m/min.

2.2 Preparation of HA/CS composite scaffold

A 1.0 g sample of CS powder (deacetylation degree: 85%, M_η: 4×10^5) was dissolved in 100 mL of acetic acid solution (2.0

wt%). 2.3615 g of $Ca(NO_3)_2 \cdot 4H_2O$ and 0.9361 g of $NaH_2PO_4 \cdot 2H_2O$ were added into the above CS/acetic acid solution at room temperature. The CS fibre scaffold was immersed into the above mixed solution for 5 min, and was then withdrawn at a rate of 1 mm/s. After drying at 40°C for 48 h, DCPD/CS composite scaffold was produced. The as-obtained samples were immersed in NaOH solution (5.0wt %) at 37 °C for 24 h. Finally, the product (HA/CS composite scaffold) was dried at 40°C in a humid atmosphere.

2.3 Characterization

The morphology and microstructure of the samples were investigated using field-emission scanning electron microscopy (FESEM, Hitachi S-4800, CamScan) with energy-dispersive spectrometry (EDS). The phases of samples were examined by X-ray powder diffraction (XRD, D/max-ⅡB, Japan). The pore structure of the samples was measured by a Capillary Flow Porometer (CFP, Through-pore size analyzer, Porometer 3G zh, Quantachrome Instruments Ltd., Florida, USA).

$$P = (W_1 - W_2)/(\rho \cdot V) \qquad (1)$$

where W_1 and W_2 are the wet weight and the dry weight of the material respectively, ρ is the density of the wetting fluid (Quantachrome Instruments Ltd., Florida, USA) with a defined surface tension of 16 dynes/cm, and V is the total volume of the samples.

2.4 Mechanical properties

The mechanical properties of the samples, including the compression properties, flexure properties and tensile properties, were analyzed with different test instruments. The compression properties were measured by a universal material testing machine 2T (WDW3020, Changchun New Test Instrument Co., Ltd., China) with a compression speed of 0.5mm/min and a specimen size of 25 mm long, 25 mm wide, and 30 mm thick. The flexure properties were measured by a microcomputer control electronic universal testing machine (WDW-20, Shanghai Hualong Microelectronics Co., Ltd., China) with a chuck travelling speed of 1 mm/min and a specimen size of 50 mm long, 20 mm wide, and 3 mm thick. The tensile properties were measured by an electrical universal material testing machine (YG028-500, Changzhou First Textile Machinery Co., Ltd., China) with a stretching velocity of 10 mm/min and a gauge length of 40 mm. The size of the samples was 50 mm long, 20 mm wide and 3 mm thick. Each measurement was performed three times.

2.5 Cell behaviour

2.5.1 Cell culture

All protocols for human bone marrow were approved by the Research Ethical Committee of Shanghai Jiao Tong University Affiliated Sixth People's Hospital. Donors were healthy with no metabolic, inherited or other diseases that might affect the current study. All participants signed the informed consent. Growth media was prepared α-MEM supplemented with 10% fetal bovine serum (FBS, Hyclone). Human bone marrow stromal cells (hBMSCs) were isolated and expanded as previously described.[30] Cells were incubated at 37°C in a 5% CO_2 incubator, and the media were changed every 3 days. After 7 days of primary culture, cells were detached using trypsin/EDTA (0.25% w/v

trypsin/0.02% EDTA) and plated onto 100-mm dishes.

Before cells were seeded, scaffolds with a thickness of 3 mm were cut into 15 mm disks. In order to sterilize the scaffolds, they were soaked in 75% ethanol for 2 h, followed by rinsing with PBS to remove the residual ethanol. Then, the scaffolds were transferred into 24-well plates. A total of 2×10^4 hBMSCs were seeded on two different scaffolds. The cells were allowed to adhere to the scaffold for 3 h, and then DMEM with 10% FBS was added.

2.5.2 Cell morphology

For the cell morphology analysis, the constructs were cultured for 24 h and fixed with 4% paraformaldehyde for 30 min at room temperature. The specimens were then rinsed in 0.1% Triton X-100 solution for 15 min. Then, actin filaments of cells were stained with 20 μg/ml of phalloidin (Cytoskeleton, US) for 30 min at room temperature according to instructions of the manufacturer. Finally, cells were stained with 4', 6-diamidino-2-phenylindole (DAPI) for 5 min at room temperature. The cytoskeleton of hBMSCs was imaged using a confocal laser scanning microscope (CLSM) (Leica, Germany).

2.5.3 Cell proliferation assay

The cell proliferation on the scaffolds was performed using CCK-8 according to the manufacturer's instructions. 100 μL of CCK-8 reagent was added to culture plates and incubated at 37^oC in a 5% CO_2 incubator for 2 h. A 200 μL of the mixture was transferred to 96-well plates and measured for absorbance at 450 nm. Non-seeded scaffolds were analyzed as blank controls, which were then subtracted from the corresponding samples.

2.5.4 ALP activity

The levels of hBMSCs differentiation in the scaffolds were assessed based on ALP activity after the cells were cultured with α-MEM with 10% FBS for 7 and 14 days. ALP activity was measured using an ALP kit (Jiancheng, China) as previously described.[31] Briefly, the scaffolds were washed with PBS three times. The scaffolds were then soaked in 0.01% Triton-100 to dissolve cells. The mixture was centrifuged at 14,000 rpm for 15 min at 4℃. The supernatant was transferred to an EP tube, and ALP working solution was added. After incubation at 37^oC for 15 min, 1N NaOH was added to stop the reaction. The absorbance at 450 nm was measured using an iMarkMicroplate Absorbance Reader (Bio-RAD).The total protein content was then measured using the bicinchoninic acid (BCA) assay kit. The ALP activities were normalized to the total protein content. All experiments were conducted in triplicate.

2.5.6 Alizarin red staining

Alizarin red staining was used to detect calcium deposits by cells in culture as previously described.[32] After 14 days of culture, the cell-seeded scaffolds were washed with PBS, fixed with formaldehyde for 15 min and then stained with 1mL of 40nM alizarin red (pH=4.1) for 30 minutes. The scaffolds were then thoroughly washed with PBS to remove the unbound dye. To dissolve the bound dye, the constructs were placed in 1.5 mL 50% acetic acid solution for 24 h at room temperature. The solution was then added to 1.5-mL tubes containing 600 μL of 1M NaOH to adjust the pH to 4.1. The solution was then transferred to a 96-well plate, and the absorbance was measured at 550 nm using a microplate reader (iMark^TM; Bio-Rad)

2.6 *In vivo* implantation

2.6.1 Animal experiments

All animal experiments were approved by the Shanghai Jiao Tong University Affiliated Sixth People's Hospital. Eighteen adult male Sprague-Dawley (SD) rats (12 weeks old, 250-300 g) were used in this study, and the surgical procedure was performed as previously described.[33] Briefly, the rats were anesthetized with 10% chloral hydrate (350mg/kg, intraperitoneal injection). The surgical area was shaved and sterilized with iodophor. A 15-mm-longincision was made on the skull, and the calvarium was exposed by blunt dissection. Two 6 mm full-sickness bone defects were created by a dental drill. The bone defects were created under constant irrigation with 0.9% saline to prevent overheating and to remove the debris. After rinsing in PBS for 10 min, the CS fibre porous scaffold (*n*=6) or HA/CS composite scaffold (*n*=6) were randomly placed into the defects site. Six rats were filled with nothing and served as the blank control. The incision was closed using 4-0 resorbable sutures. The rats were allowed to recover under a warm lamp and were able to function normally after this procedure.

2.6.2 Sequential fluorescent labeling

A polychrome sequential fluorescent labelling method was performed as previously described.[34] After 4 and 6 weeks of the implantation, the rats were subjected to an intraperitoneal injection of fluorochromes as follows: calcein (10mg/kg; Sigma) and alizarin red (20mg/kg; Sigma).

2.6.3 Micro-CT tomography

The animals were killed after 8 weeks of post-surgery. The skulls were fixed in 10% neutral formalin. The calvarial defects were scanned using a high-resolution micro CT system (Skyscan, Belgium). The scan conditions were set as follows: 180° rotation angle with a rotation step of 0.6° at 18 μm resolution. The histomorphometric analysis was performed using NRecon Software to measure the bone volume. After scanning, the new bone was reconstructed by software for three-dimensional isosurface renderings. The percentages of the new bone volume relative to tissue volume (BV/TV) and the bone mineral density (BMD) were calculated using the software.

2.6.4 Fluorescent and histological observation

After dehydration in a graded series of alcohol, the undecalcified samples were embedded in polymethylmethacrylate (PMMA). The specimens were cut, hand ground and polished to a final thickness of approximately 40 μm. Undecalcified sections were observed by fluorescent labelling using a CLSM. The excitation/emission wavelengths of the fluorochromes used were 543/580-670 nm (alizarin red, red) and 488/500-550 nm (calcein, green). The undecalcified sections were then stained with van Gieson's picrofuchsin for histological observation.

2.7 Statistical analysis

The results are presented as the means ± SD. The statistical analysis was conducted by analysis of variance (ANOVA), and non-parametric analysis was performed by Wilcoxon-Mann-Whitney. All experiments were performed in sextuplicate. (*) and (**) denotes significant difference with $P < 0.05$.

3. Results and discussion

3.1 Characterization and formation mechanism of HA/CS composite scaffold

The biomineralization mechanism of bone minerals indicates that apatite nanocrystals are converted from ACP by using metastable crystalline phases such as octacalcium phosphate (OCP, $Ca_8H_2(PO_4)_6 \cdot 5H_2O$) and brushite (DCPD, $CaHPO_4 \cdot 2H_2O$) as transitory precursors, resulting in the formation of hybrid nanostructured collagen/apatite composites.[9] In this work, we mimicked the biomineralization process of the apatite in bone tissue to fabricate hybrid nanostructured HA/CS composite scaffold with HA nanorods perpendicularly oriented to CS fibres, as shown in Scheme 1.
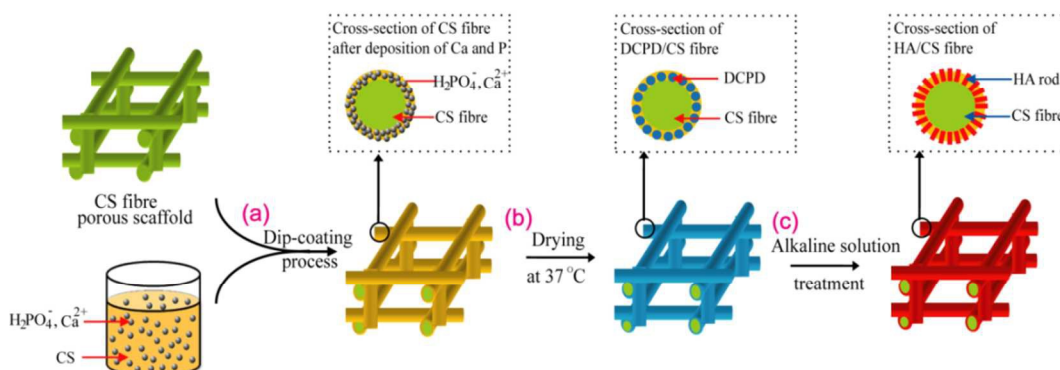
Scheme 1. Illustration of the fabrication process of hybrid nanostructured HA/CS composite scaffold: (a) deposition of CS precursors including Ca^{2+} and $H_2PO_4^-$ ions on CS fibre porous scaffold by a dip-coating method; (b) formation of DCPD/CS composite scaffold after drying at $37\,^{\circ}C$; (c) conversion of HA/CS composite scaffold from DCPD/CS composite scaffold by alkaline solution treatment.
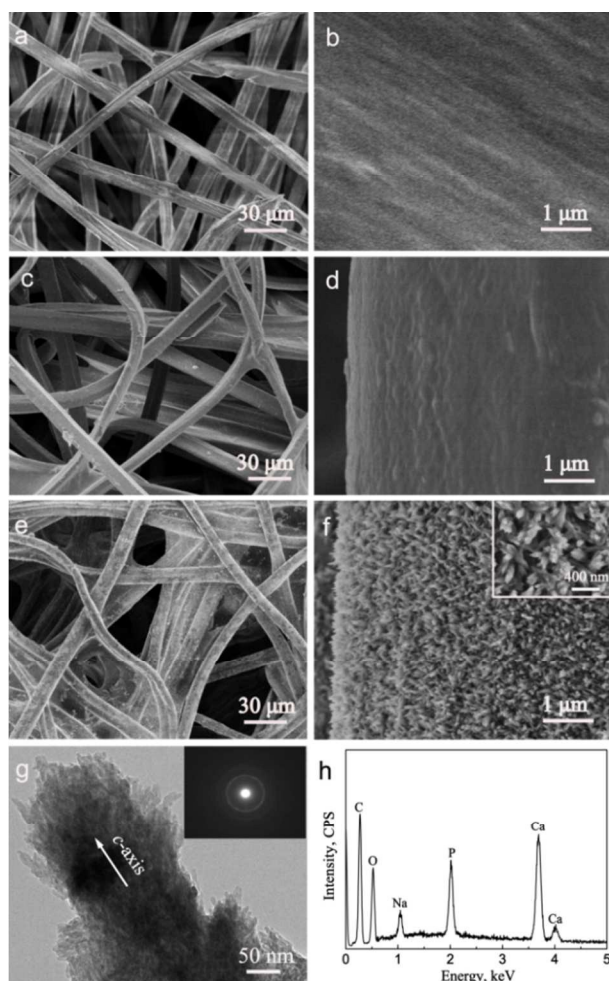

Fig. 1. FESEM images of different samples: (a, b) CS fibre porous scaffold, (c, d) DCPD/CS composite scaffold, (e, f) HA/CS composite scaffold; (g) TEM image of HA/CS composite scaffold; (h) EDS spectrum of HA/CS composite scaffold.

At the first stage, the CS precursors including Ca^{2+} and PO_4^{3-} ions deposited on CS fibre porous scaffold by a dip-coating process (Scheme 1a). The CS fibre porous scaffold as-fabricated by a needle-punching method possesses 3D interconnected macroporous structure, and the CS fibre has a uniform diameter of approximately 15 μm (Fig. 1a). The pore sizes are mainly attributed around 80-120 μm, as confirmed by the corresponding pore size distribution curve in Fig. 2a. The precursors including CS, Ca^{2+} ions and $H_2PO_4^-$ ions were prepared by the addition of $Ca(NO_3)_2 \cdot 4H_2O$ and $NaH_2PO_4 \cdot 2H_2O$ into CS/acetic acid solutions. Since $Ca(NO_3)_2$ and NaH_2PO_4 can be dissolved in acetic acid solutions, no calcium phosphate phases exist in the mixtures solutions. After deposition of precursors on the CS fibre porous scaffold, the calcium and phosphorus exist as ion states.
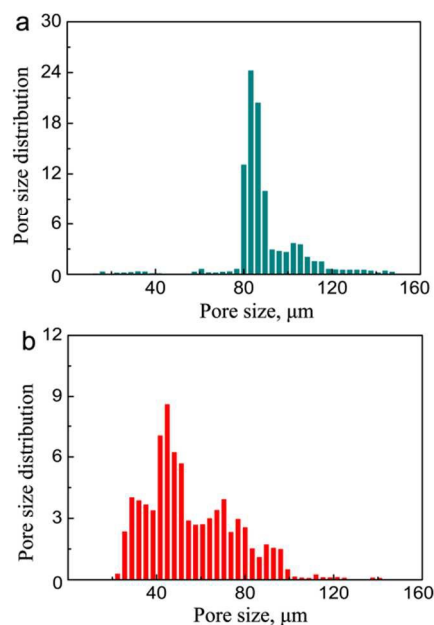

Fig. 2. Pore size distribution curves of the samples: (a) CS fibre porous scaffold; (b) HA/CS composite scaffold

At the second stage, DCPD/CS composite scaffold was formed by the *in situ* deposition of DCPD on the CS porous scaffold after drying at 37°C for 48 h (Scheme 1b). Because H_3PO_4 is a weak acid, the ionization reactions of $H_2PO_4^-$ ions occur according to 5 the following equations:

$$H_2PO_4^- \rightarrow HPO_4^{2-} + H^+ \tag{2}$$

$$HPO_4^{2-} \rightarrow PO_4^{3-} + H^+ \tag{3}$$
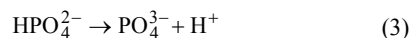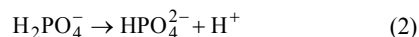
The percentages of $H_2PO_4^-$, HPO_4^{2-} and PO_4^{3-} ions in the solution depend on pH values. After drying at 37°C, the acetic 10 acid may volatilize. The volatilization of acetic acid increases the pH value, and the ionization products ($H_2PO_4^-$ ions) will react with Ca^{2+} ions and H_2O to form DCPD.

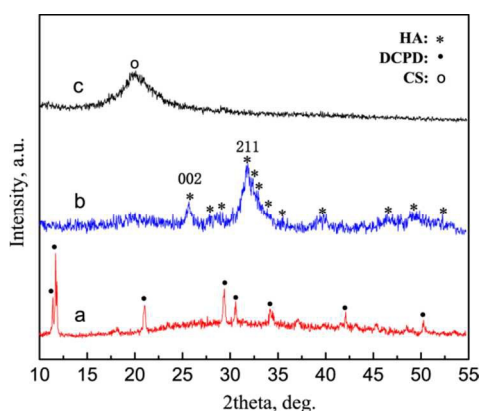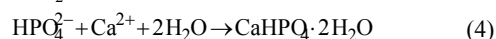$$HPO_4^{2-} + Ca^{2+} + 2H_2O \rightarrow CaHPO_4 \cdot 2H_2O \tag{4}$$

15 **Fig. 3.** XRD patterns of the samples: (a) DCPD/CS composite scaffold; (b) HA/CS composite scaffold; (c) CS.
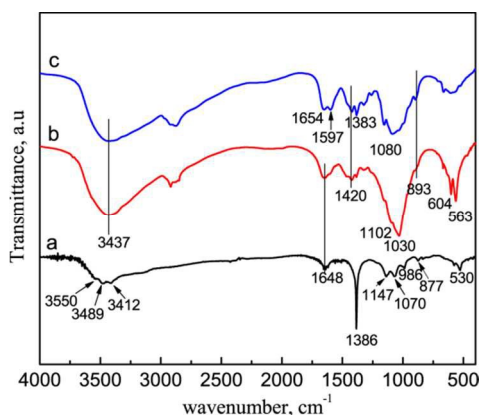

Fig. 4. FTIR spectra of the samples: (a) DCPD/CS composite scaffold; (b) HA/CS composite scaffold; (c) CS.

20 The XRD pattern in Fig. 3a indicates the characteristic peaks of DCPD in the DCPD/CS composite scaffold. The functional groups of DCPD are demonstrated by FTIR spectrum in Fig. 4a. The infrared stretching $\nu(OH)$ are observed at 3550, 3489 and 3412 cm^{-1}. The band at 1648 cm^{-1} is ascribed to the H-O-H 25 bending of lattice water molecules.[35] The bands at 1147, 1070, 986 and 877 cm^{-1} are ascribed to P-O stretching vibration in HPO_4^{2-} groups, respectively.[35] The band due to O-P-O(H) bending mode locates at 530 cm^{-1}. Notably, the DCPD/CS

composite scaffold possesses smooth surfaces similar to the CS 30 porous scaffold (Figs. 1a-d), because the DCPD particles are covered with CS.

At the final stage, HA/CS composite scaffold with HA nanorods perpendicularly oriented to CS fibres was converted from DCPD/CS composite scaffold after alkaline solution 35 treatment (Scheme 1c). The weight percent of the HA in the HA/CS composite scaffold is about 35.2 wt%, which was determined by thermo-gravimetric analysis. The CS porous scaffold possesses 3D interconnected macroporous structure (Fig. 1a). After deposition of HA nanocrystals on its surfaces, the 40 macropores are remained (Fig. 1e). As compared with the CS porous scaffold, the HA/CS composite scaffold has the smaller pore size of around 30-100 μm because the macropores are partly filled with HA crystals (Fig. 2). The high-resolution SEM image shows many HA rods are distributed homogeneously on the 45 entire surface of the CS fibre porous scaffold (Fig. 1f). These HA rods with a length of ~300 nm and width of ~80 nm are perpendicularly oriented to the CS fibres. Interestingly, the TEM image in Fig. 1g that the HA rods possess the hierarchical nanostructure, which are composed of many smaller nanorods 50 oriented along the *c*-axis orientation. The length and width of the nanorods is ~40 nm and ~10 nm, respectively. This hierarchical nanostructure is much similar to the biological apatite in bone tissue. In natural bone, the apatite crystals with a length of 30-50 nm, width of 15-30 nm and thickness of 2-10 nm exhibit *c*-axis 55 orientation, too.[36-38] The corresponding EDS spectrum reveals that the chemical elements of the HA/CS composite scaffold mainly include Ca, P, O, C and Na. Ca, P, O are derived from HA, C is derived from CS, and Na is mainly due to the adsorption of Na$^+$ ions on the scaffold or the substitution of the Ca^{2+} ions in 60 HA crystal lattice by Na$^+$ ions. The average Ca/P molar ratio of HA in the scaffold is approximately 1.53, which is lower than that of stoichiometric HA (1.67), indicating that as-obtained HA is calcium deficient.

The phase structures and functional groups of the HA/CS 65 composite scaffold were characterized by using XRD pattern and FTIR spectrum, and the CS porous scaffold served as a control sample. CS, a random copolymer of N-acetyl-D-glucosamine and D-glucosamine, is the partially de-acetylated derivative of chitin. For the CS fibre porous scaffold, the broad peak at $2\theta=20.6°$ is 70 attributed to CS because it is a semi-crystalline material (Fig. 3a). The functional groups of the CS porous scaffold are detected by FTIR spectrum in Figure 4c. The band at 1597 cm^{-1} is assigned to the N-H bending vibration overlapping the amide II vibration. C-N stretching vibration occurs at around 1030 cm^{-1} and overlaps 75 the vibration from the carbohydrate ring. The broad band at around 3437 cm^{-1} is corresponding to the stretching vibration of N-H and OH groups. The band at 1654 cm^{-1} is attributed to the axial C=O stretching of the acetamido groups (named amide I). The bands at 1420 and 1383 cm^{-1} are ascribed to -CH$_2$ bending 80 vibration and the -CH$_3$ symmetrical deformation mode, respectively.[39-41] For the HA/CS composite scaffold, the characteristic peaks due to HA crystals are detected in the XRD pattern (Fig. 1c). The broad peaks and low peak strengths indicate that the HA crystals in the scaffold possess a low crystallinity, 85 which is much similar to that of biological apatite.[42] As compared with the standard diffraction pattern (JCPDS card no. 09-0432),

the intensity ratio between the (002) and (211) diffraction is stronger, suggesting the preferential growth of the HA along the *c*-axis. The functional groups of both CS and HA are observed in the FTIR spectrum of the HA/CS composite scaffold (Fig. 4c). The intense absorption peak at 1030 cm^{-1} is ascribed to the stretching vibration (v_3) of the phosphate (PO_4^{3-}) groups, and the absorption peaks at 563 and 604 cm^{-1} are ascribed to the bending vibration (v_4) of the phosphate (PO_4^{3-}) groups.[42] The absorption band due to HPO_4^{2-} at around 1102 cm^{-1} indicates that the samples are calcium-deficient HA.[43] The band at 3437 cm^{-1} is corresponding to OH group in HA crystals or adsorbed water on the composite scaffold.[44] The characteristic bands of CS at 1420, 1654 and 1383 cm^{-1} are observed in the HA/CS composite scaffold (Fig. 4c). However, its characteristic bands at 1080 and 3437 cm^{-1} are overlapped by those of HA crystals (Fig. 4b).

The above results of the SEM images, XRD patterns and FTIR spectra reveal that the DCPD/CS composite scaffold are converted into the HA/CS composite scaffold after treatment with the NaOH solution. The different morphology of the DCPD/CS composite scaffold from the HA/CS composite scaffold (Figure 1) suggests that the conversion mechanism is a dissolution-precipitation reaction. Since the logarithmic solubility product of DCPD (pK_{sp}=6.622) is lower than that of HA (pK_{sp}=58.6), HA is more stable in solutions than DCPD.[45] After soaking the DCPD/CS composite scaffold in the NaOH solution, the Ca^{2+} and PO_4^{3-} ions are dissolved from the DCPD in the scaffold according to the following equation:

$$CaHPO_4 \cdot 2H_2O + OH^- \rightarrow Ca^{2+} + PO_4^{3-} + 3H_2O \quad (5)$$
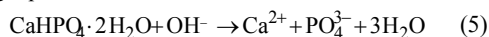
The released Ca^{2+} and PO_4^{3-} ions may react with the OH^- ions in the NaOH solution to produce HA particles as the ionic activity product exceeds the thermodynamic solubility product.

$$10Ca^{2+} + 6PO_4^{3-} + 2OH^- \rightarrow Ca_{10}(PO_4)_6(OH)_2 \quad (6)$$
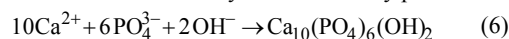
The SEM and TEM images indicate that the hierarchically nanostructured HA rods deposit on the scaffold surfaces, and are perpendicularly oriented to the CS fibres with *c*-axis orientation (Fig. 1f). The formation of hybrid nanostructured HA rods with oriented crystallographic texture may be attributed to the following reasons. Firstly, the Ca^{2+} and PO_4^{3-} ions are mainly released from the DCPD in the DCPD/CS composite scaffold (Eq. 3), so the concentrations of Ca^{2+} and PO_4^{3-} ions exhibit gradient distributions and decrease gradually from the CS fibre to solution. The gradient distributions of Ca^{2+} and PO_4^{3-} ions tend to promote the deposition of HA crystals perpendicularly oriented to the CS fibres. In addition, the functional groups of CS such as –OH and -NH_2 in the DCPD/CS composite scaffold may serve as active sites, which accelerate the HA nucleation rather than crystal growth. The functions of CS on the formation of hierarchically nanostructured HA are similar to collagen in bone tissue. Nudelman et al. have indicated the collagen functions in synergy with inhibitors of HA nucleation to actively control mineralization. The clusters of charged amino acids, both in gap and overlap regions, form nucleation sites controlling the conversion of ACP into a parallel array of oriented apatite crystals.[9]

Table 1 Mechanical properties of the CS fibre porous scaffold, HA/CS composite scaffold and trabecular bone.

Samples	Compression Strength (MPa)	Elastic modulus (GPa)	Flexure Strength(MPa)	Flexure modulus (GPa)	Tensile Strength (MPa)	Tensile Modulus(MPa)
CS fibre porous scaffold	-	-	-	-	0.68 ± 0.06	3.40 ± 0.24
HA/CS composite scaffold	9.41 ± 1.63	0.17 ± 0.02	7.79 ± 0.70	0.38 ± 0.02	3.12 ± 0.12	73.67 ± 3.51
Trabecular bone[48]	4 - 12	0.1 - 0.5				

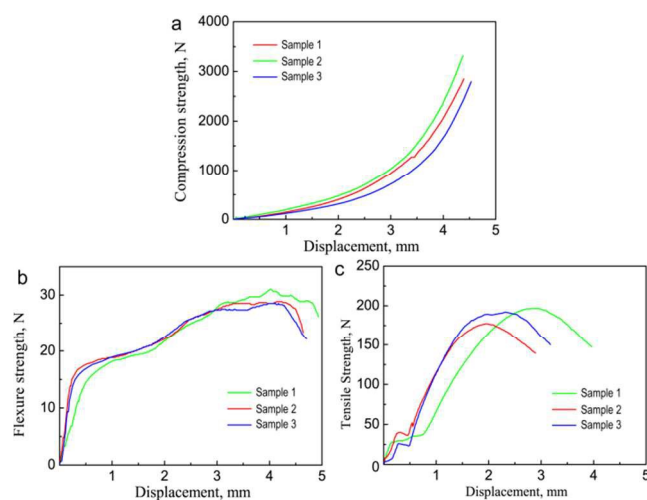## 3.2 Mechanical properties of HA/CS composite scaffold

Fig. 5. Mechanical response in (a) compression, (b) tensile and (c) flexure for HA/CS composite scaffold: Sample 1, 2, 3 were fabricated under the same conditions.

Bone scaffolds for repairing large segmental bone defects should possess good mechanical properties, especially under load-bearing conditions. Fig. 5 shows the relation curves of the mechanical strength and displacement for the HA/CS composite scaffold, including the compression strength, flexure strength and tensile strength. The composite samples tested in this study are fabricated under the same conditions. From the relation curves, we can determine the ability of the materials to sustain loads without undue distortion or failure. The mechanical parameters of the samples are summarized in Table 1. The HA/CS composite scaffold has a compression strength of 9.41±1.63 MPa and elastic modulus of 0.17±0.02 GPa, which match the compression performance of trabecular bone. In addition, the HA/CS composite scaffold has strong flexure properties with a tensile strength of 3.12±0.12 MPa. In contrast, the CS fibre porous scaffold as a soft ductile material has good tensile properties, but exhibits poor compression and flexure properties. When compressed by an external force, the scaffold undergoes compression deformation only, without a brittle fracture process. Therefore, the CS fibre porous scaffold has no compression or flexure properties. The good mechanical properties of the HA/CS composite scaffold are attributed to its hybrid nanostructured composite material. Pure HA is a brittle material with low

fracture toughness, while pure CS fibre is a soft ductile material with low mechanical strength. Interestingly, the HA/CS composite scaffold combines the strong hardness of HA crystals with the good tensile property of CS fibres. In addition, natural

5 bone is a nanostructured architecture consisting of uniaxially oriented HA nanocrystals embedded in collagen matrix, which gives bone the unique mechanical properties to withstand dynamic loading.[46,47] Therefore, we can infer that the hybrid nanostructures with the HA nanorods perpendicularly oriented to

10 CS fibres tend to increase the mechanical properties of the HA/CS composite scaffold.

3.3 Cell performances of hBMSCs on HA/CS composite scaffold

Ideal bone scaffolds must have excellent biocompatibility with

15 surrounding cells and tissues, which do not elicit any undesirable effects on the host and promote satisfactory osteointegration between the implant and bone tissue.[49] The cytocompatibility of HA/CS composite scaffold was investigated by using hBMSCs as cell models and CS fibre porous scaffold as control sample. The

20 hBMSCs are the most widely used stem cells in bone tissue regeneration.[50,51] Porous scaffold loaded with hBMSCs represent a promising approach for the treatment of critical size bone defects.[52-54] Fig. 6 shows the CLSM images of hBMSCs cultured on the CS fibre porous scaffold and HA/CS composite scaffold

25 for 1 day. The cells on both scaffolds exhibit typical fibroblast-like morphology. They attach to the scaffolds with filopodia and connect with each other with fibrillar matrix. The above results suggest that both the CS fibre porous scaffold and HA/CS composite scaffold can promote the adhesion and spreading of
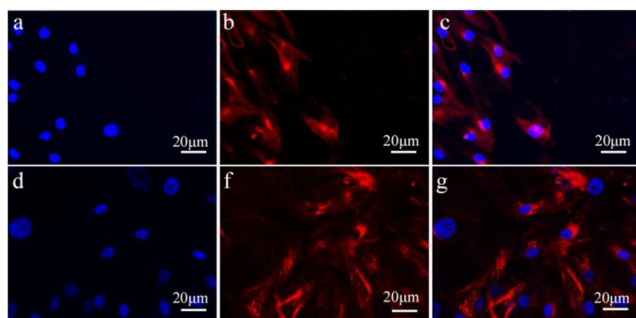
30 the cells.

Fig. 6. CLSM images of hBMSCs cultured on different samples for 1 day: (a-c) CS fibre porous scaffold; and (d-f) HA/CS composite scaffold.

CCK-8 assays were performed to investigate the proliferation

35 of hBMSCs on the HA/CS composite scaffold and CS fibre porous scaffold. Fig. 6a indicates the increasing trend of cell proliferation in a time-dependent manner is observed for both samples. Interestingly, the number of viable cells on the HA/CS composite scaffold is more than on the CS fibre porous scaffold

40 over the whole period, suggesting that the HA/CS composite scaffold has higher capability to promote the proliferation of hBMSCs. The CLSM images and CCK-8 assay results demonstrate that both the HA/CS composite scaffold and CS fibre porous scaffold have good cytocompatibility, which can

45 promote the adhesion, spreading and proliferation of hBMSCs. Notably, the more viable cells are detected on the HA/CS composite scaffold than on the CS fibre porous scaffold during

the whole examination period, which may be attributed to the presence of nanostructured HA rods with preferential *c*-axis

50 orientation in the composite scaffold. Biological apatite is a natural bone mineral component, and the corresponding HA has excellent bioactivity and biocompatibility. The incorporation of HA enhances the cytocompatibility of the HA/CS porous scaffold and provides a suitable environment for cell proliferation. In

55 addition, the *c*-axis oriented HA nanorods on the CS fibres may support the adhesion, proliferation of the hBMSCs.[18]
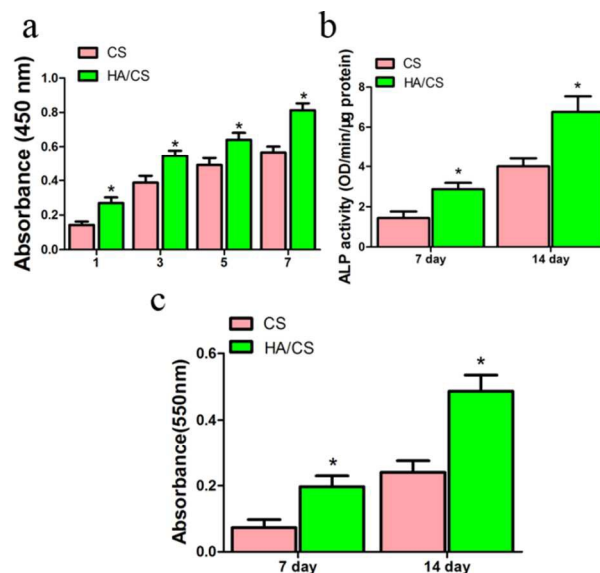

Fig. 7. (a) Proliferation of hBMSCs on CS fibre porous scaffold and HA/CS composite scaffold at different times; (b) ALP activity of
60 hBMSCs cultured on CS fibre porous scaffold and HA/CS composite scaffold after 7 and 14 days. (c) Absorbance of alizarin red staining values. The data are represent as the means ± standard deviation; *n*=6 (*$p<0.05$)

Bone scaffolds should not only have good cytocompatibility,

65 but also exhibit excellent osteoinductivity. The osteogenic differentiation of hBMSCs on the HA/CS composite scaffold was investigated by using the CS fibre porous scaffold as control group. In the process of hBMSCs osteogenesis, ALP is an early marker for osteoblast differentiation, which involves the

70 degradation of inorganic pyrophosphate to provide sufficient local concentrations of phosphate for mineralization.[55] The increased ALP activity suggest the osteogenic differentiation of hBMSCs. Fig. 7b shows the relative ALP activity of the hBMSCs on the HA/CS composite scaffold and CS fibre porous scaffold at

75 7 and 14 days. Both groups exhibit a similar time-dependent increase in ALP activity from 7 days to 14 days. The hBMSCs on the HA/CS composite scaffold have the higher ALP levels than those on the CS fibre porous scaffold throughout the entire study, suggesting that the HA incorporation induced a significant up-

80 regulation of ALP expression.

The calcium mineralization is a marker for osteogenic differentiation, too.[56] In order to detect the calcium deposition, the cell-scaffold constructs were stained with alizarin red. The quantitative analysis of alizarin red staining in Fig. 7c shows that

85 the HA/CS composite scaffold has higher absorbance values than the CS fibre porous scaffold, suggesting that there is more mineral deposition on the HA/CS composite scaffold. To confirm

that this calcium is deposited by hBMSCs and not due to the HA layer in the HA/CS composite scaffold, the HA/CS composite scaffold was detected without hBMSCs, and no deposition is found. The calcium deposition demonstrates the osteogenic differentiation of hBMSCs on the HA/CS composite scaffold. The above data suggest that the HA/CS composite scaffold significantly promotes the osteogenic differentiation of hBMSCs. The better osteoinductivity of the HA/CS composite scaffold than the CS fibre scaffold may be attributed to their unique chemical component, morphology and crystallographic texture. Firstly, the HA crystals in the HA/CS composite scaffold have the similar low crystallinity and particle size to the apatite crystals in natural bones, as demonstrated by SEM images, XRD patterns and FTIR spectra (Figs. 1, 3 and 4). The proper calcium and phosphate microenvironment of the HA/CS composite scaffold stimulates osteogenic differentiation of stem cells.[48] Secondly, the mechanical parameters of the HA/CS composite scaffold are similar to trabecular bone. The appropriate mechanical properties of HA/CS composite scaffold not only increase the cell attachment and proliferation, but also stimulate the osteogenic differentiation of hBMSCs.[57] Thirdly, HA with surfaces exhibiting a tailored crystallographic texture may enable a new level of control of cellular behaviour. Liu et al. have reported that the ordered fluorapatite crystal surfaces can; stimulate the expression of a set of pro-osteogenic transcripts and bone mineralization phenotypic markers of adipose-derived stem cells as compared to metal surfaces.[18] For the HA/CS composite scaffold, we can infer that the HA c-axis orientation to the CS fibres may enhance the osteogenic differentiation of stem cells, too.

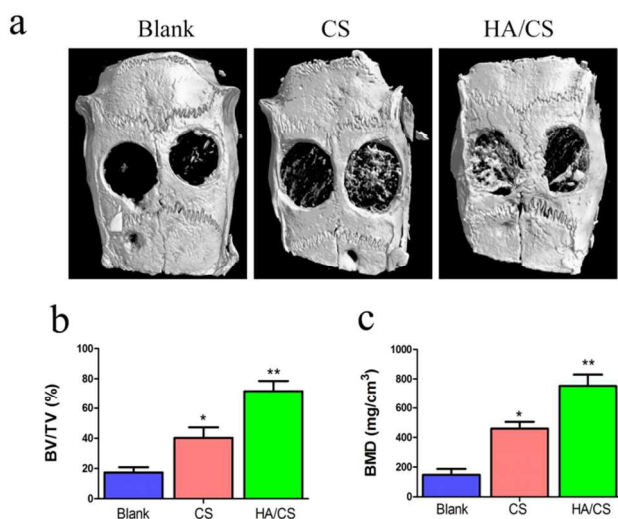### 3.4 Bone regeneration in HA/CS composite scaffold

Fig. 8. (a) Micro-CT images of defects implanted with blank control, CS fibre porous scaffold and HA/CS composite scaffold after 8 weeks; (b) Morphometric analysis (BV/TV) of new bone formation and (c) local BMD analysis for three groups in the defect site. The data are represent as the means ± standard deviation; n=6. (*P<0.05: CS fibre porous scaffold compared with the blank control group; **P<0.05: HA/CS composite scaffold compared with CS fibre porous scaffold or blank control group)

A critical-sized calvarial defect is a widely used model to investigate the process of bone regeneration.[58] Herein, we implanted the HA/CS composite scaffold and CS fibre porous scaffold into critical-sized calvarial bone defects. Micro-CT images of defects implanted with the different groups of scaffolds after 8 weeks are shown in Fig. 8a. Defects filled with blank control and CS fibre porous scaffold fail to show any appreciable new bone formation. Interestingly, the majority of the cranial defects are filled with substantial newly formed bone tissue in the defect site treated with the HA/CS composite scaffoldafter8 weeks of implantation. To quantify the new bone regeneration within the calvarial defects, BV/TV and local BMD were measured and compared with normal calvarial bone. BV/TV is an indicator of the relative amount of newly formed bone. Significantly greater BV/TV is observed in the HA/CScomposite scaffold group (66.7±12.1%) than the CS fibre porous scaffold group (37.7±9.6%) or blank control group (17.3±6.1%). Moreover, the BMD of the HA/CS composite scaffold group (759.7±93.1 mg/cm^3) is significantly higher than the CS fibre porous scaffold group (433.2±50.8 mg/cm^3) or the blank control group (149.7±57.1 mg/cm^3). These results reveal that the HA/CS composite scaffold markedly enhance bone regeneration.
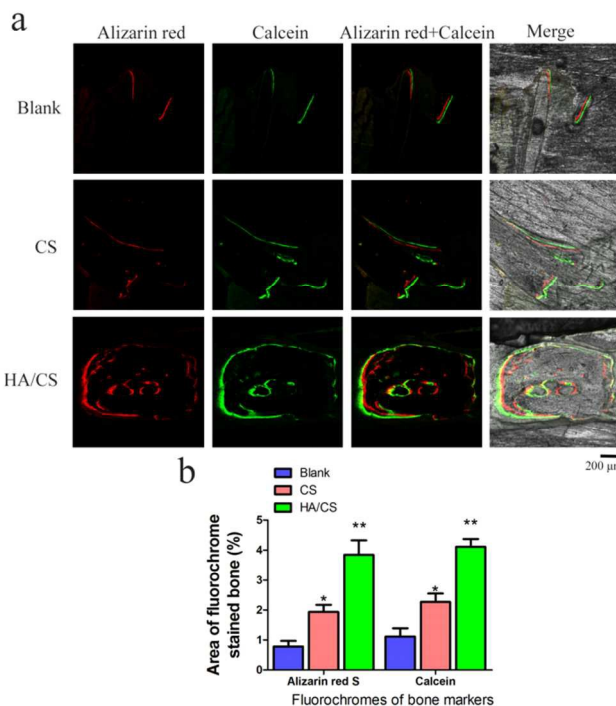

Fig. 9. Fluorescent labelling of new bone formation and mineralization for blank control, CS fibre porous scaffold and HA/CS composite scaffold after 4 and 6 weeks: (a) Row 1 (red) shows the deposition of alizarin red at week 4, row 2 (green) shows the deposition of calcein at week 6, row 3 shows the merged images of the two fluorochromes for the same group, and row 4 shows the merged images of the two fluorochromes with a plain CLSM image for the same group. Scale bar = 200 μm. (b) The graph represents the percentages of the two fluorochromes area for the three groups. (*P<0.05: CS fibre porous scaffold compared with the blank control group; **P<0.05: HA/CS composite scaffold compared with CS fibre porous scaffold or blank control group)

Sequential bone formation and mineralization was analyzed histomorphometrically by alizarin red and calcein fluorescence quantification, which represented the mineralized bone matrix at different time intervals (Fig. 9a). After 4 weeks, the percentages of alizarin red labelling are 0.8 ± 0.1%, 1.4 ± 0.2% and 3.5 ± 0.3% for the blank control, CS fibre porous scaffold and HA/CS

composite scaffold groups, respectively (Fig. 9b). The fluorescent-labelling areas in HA/CS composite scaffold group are larger than those in the blank control or CS fibre porous scaffold groups. After 6 weeks, the percentages of calcein labelling areas are $1.1 \pm 0.2\%$, $1.6 \pm 0.1\%$ and $3.7 \pm 0.2\%$ for the blank control, CS fibre porous scaffold and HA/CS composite scaffold groups, respectively (Fig. 9b), and shows the same pattern as the alizarin red.
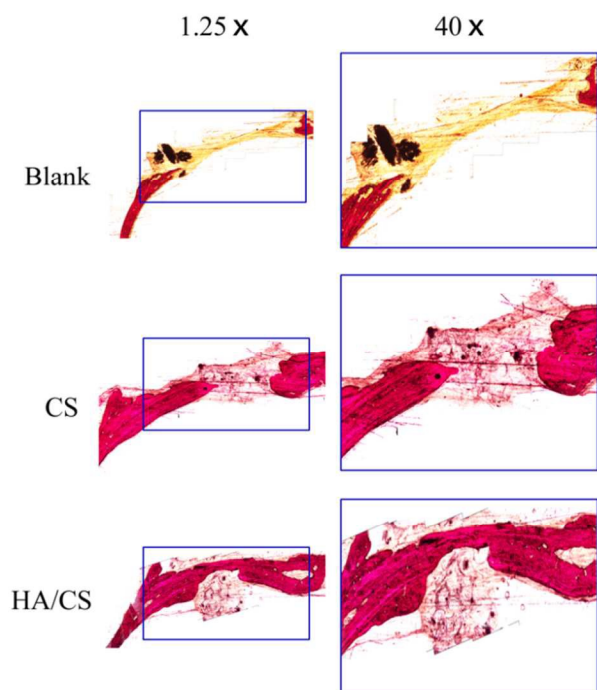

Fig. 10 Histological analysis of newly formed bone in calvarial defects filled with the blank control, CS fibre porous scaffold and HA/CS composite scaffold after 8 weeks.

Fig. 10 shows the van Gieson's picrofuchsin staining of the decalcified sections for the blank control, CS fibre porous scaffold and HA/CS composite scaffold groups. The HA/CS composite scaffold group shows nearly complete osseous closure of the defect, where the newly formed bone has a typical organized and mature bone morphology similar to native bone. In contrast, histological analysis indicates a small amount of irregularly arranged bone tissue and less bone formation in the CS fibre porous scaffold group. Especially, no new bone formation is observed in the blank control group. The histological evidence further supports the micro-CT and fluorochrome labelling results, suggesting that the HA/CS composite scaffold group has significantly more mineralized tissue than the CS fibre porous scaffold or blank control groups.

Taken together, the above data in Figs. 8-10 indicate that the HA/CS composite scaffold effectively promotes new bone regeneration and mineralization. The reasons may be attributed to the chemical components, crystallinity, crystallographic texture and microstructure of the composite scaffold. Firstly, the hybrid composite scaffold is composed of CS and HA. CS originated from hard shell of insects and crustaceans has good cytocompatibility, biodegradability and bioactivity.[59-61] Notably, the HA crystals in the HA/CS composite scaffold is similar to the mineral of natural bone. The HA has hierarchical nanostructures constructed by nanorods with a length of~40 nm and width of ~10 nm, and possessed a low crystallinity (Fig. 1g and 3b). The nanostructure and low crystallinity of HA make it have proper biodegradability. After implantation in the bone defects, the released Ca^{2+} and PO_4^{3-} ions from HA crystals support the formation of new bone. Secondly, the HA in the hybrid HA/CS composite scaffold exhibits a tailored crystallographic texture with the HA *c*-axis orientation perpendicularly to CS fibres. Kim et al. have reported that the *c*-axis texture may promote preferentially oriented growth of apatite through a cyclic process of dissolution and reprecipitation, followed by homoepitaxial growth. The *in vitro* tests suggest that highly textured HA has a capability as a bone tissue engineering scaffold.[20] Finally, the HA/CS composite scaffold possesses 3D interconnected porous structure with the pore size of 30-100 μm (Figs. 1e and 2). The macropores allow the ingrowth of bone tissue to achieve full integration with the living bones,[22] and thus the newly formed bone tissue is dispersed throughout the cranial defects after 8 weeks (Fig. 8). In addition, the HA/CS composite scaffold has good mechanical properties well-matched to those of trabecular bone (Fig. 5 and Table 1), which promote the ingrowth of bone tissue with no collapse of the scaffold.

4. Conclusion

In summary, hybrid nanostructured HA/CS composite scaffold is converted from DCPD/CS composite scaffold by a dissolution-precipitation reaction. The hybrid HA/CS composite scaffold possesses three-dimensional (3D) interconnected pores with a pore size of 30-80 μm. The hierarchically HA rods are constructed by many smaller nanorods with a length of~40 nm and width of ~10 nm, and are perpendicularly oriented to the CS fibres. Hybrid nanostructures make the composite scaffold possess exhibit good mechanical properties with compression strength of 9.41 ± 1.63 MPa and elastic modulus of 0.17 ± 0.02 GPa. *In vitro* cell tests indicate that the hybrid HA/CS composite scaffold not only supports the adhesion and proliferation of hBMSCs, but also improve the osteoinductivity. The alkaline phosphatase activity and mineralization deposition on the hybrid HA/CS composite scaffold are higher than those on the CS fibre porous scaffold. Moreover, the hybrid HA/CS composite scaffold significantly improve the formation of new bone formation in rat calvarial defects as compared with the CS fibre porous scaffold or blank control groups. Based on its excellent cytocompatibility, osteoinductivity, bone regeneration and mechanical properties, the hybrid nanostructured HA/CS composite scaffold as bone tissue engineering is promising in structural bone repair.

Acknowledgements

Shanghai Jiao Tong University School of Medicine (BXJ201341), and State Key Laboratory for Modification of Chemical Fibres and Polymer Materials, Dong Hua University.

Notes and references

[1] Y. Guo and J. Guan contributed equally to this work.

a The Education Ministry Key Lab of Resource Chemistry and Shanghai Key Laboratory of Rare Earth Functional Materials, Shanghai Normal University, Shanghai 200234, P. R. China. Fax: +86-21-64321951; Tel: +86-21-64321951; E-mail: kqf@shnu.edu.cn (Q.F. Ke) or ypguo@shnu.edu.cn (Y.P. Guo)
b Department of Orthopedics Surgery, Shanghai Jiaotong University Affiliated Sixth People's Hospital, Shanghai 20200233, China; E-mail: zhangcq@sjtu.edu.cn (C.Q. Zhang)

1 D. Sun, Y. Chen, R. T. Tran, S. Xu, D. Xie, C. Jia, Y. Wang, Y. Guo, Z. Zhang, J. Guo, J. Yang, D. Jin and X. Bai, *Sci. Rep.* 2014, **4**, 6912.
2 F. Yang, J. Wang, J. Hou, H. Guo and C. Liu, *Biomaterials* 2013, **34**, 1514-1528.
3 T. W. Bauer and G. F. Muschler, *Clin. Orthop. Relat. Res.* 2000, **371**, 10-27.
4 S. N. Khan, F. P. Jr. Cammisa, H. S. Sandhu, A. D. Diwan, F. P. Girardi and J. M. Lane, *J. Am. Acad. Orthop. Surg.* 2005, **13**, 77-86.
5 C. Szpalski, M. Wetterau, J. Barr and S. M. Warren, *Tissue Eng. Part B Rev.* 2011, **18**, 246-257.
6 Y. Hu, S. Zou, W. Chen, Z. Tong and C. Wang, *Colloid. Surface B* 2014, **122**, 559-565.
7 A. Marino, C. Filippeschi, G. G. Genchi, V. Mattoli, B. Mazzolai and G. Ciofani, *Acta Biomater.* 2014, **10**, 4304-4313.
8 W. Chen, T. Long, Y. J. Guo, Z. A. Zhu and Y. P. Guo, *RSC Adv.* 2014, **4**, 185-191.
9 M. J. Olszta, X. Cheng, S. S. Jee, R. kumar, Y. Y. Kim, M. J. Kaufman, E. P. Douglas and L. B. Gower, *Mater. Sci. Eng. R* 2007, **58**, 77-116.
10 F. Nudelman, K. Pieterse, A. George, P. H. H. Bomans, H. Friedrich, L. J. Brylka, P. A. J. Hilbers, G. deWith and N. A. J. M. Sommerdijk, *Nat. Mater.* 2010, 9, 1004-1009.
11 Z. Zhuang and M. Aizawa, *J. Mater. Sci.: Mater. Med.* 2013, **24**, 1211-1216.
12 I. Jasiuk and M. Ostoja-Starzewski, *Biomechan. Model. Mechanobiol.* 2004, **3**, 67-74.
13 A. Tatarinov and A. Sarvazyan, *IEEE T. Ultranson. Ferr.* 2008, **55**, 1287-1297.
14 A. P. Baumann, J. M. Deuerling, D. J. Rudy, G. L. Niebur and R. K. Roeder, *J. Biomech.* 2012, **45**, 2743-2749.
15 S. Miyabe, T. Nakano, T. Ishimoto, N. Takano, T. Adachi, H. Iwaki, A. Kobayashi, K. Takaoka and Y. Umakoshi, *Mater. Trans.* 2007, **48**, 343-347.
16 J. Y. Rho, M. E. Roy II, T.Y. Tsui and G. M. Phar, *J. Biomed. Mater. Res.* 1999, **45**, 48-54.
17 T. Ishimoto, T. Nakano, Y. Umakoshi, M. Yamamoto and Y. Tabata, *J. Bone Miner. Res.* 2013, **28**, 1170-1179.
18 J. Liu, X. Wang, Q. Jin, T. Jin, S. Chang, Z. Zhang, A. Czajka-Jakubowska, W. V. Giannobile, J. E. Nör and B. H. Clarkson, *Biomaterials,* 2012, **33**, 5036-5046.
19 Z. Zhuang, T. J. Fujimi, M. Nakamura, T. Konishi and H. Yoshimura, *Acta Biomater.* 2013, **9**, 6732-6740.
20 H. Kim, R. P. Camata, S. Chowdhury and Y. K. Vohra, *Acta Biomater.* 2010, **6**, 3234-3241.
21 S. Bose, M. Roy and A. Bandyopadhyay, *Trends Biotechnol.* 2012, **30**, 546-554.
22 V. Karageorgiou and D. Kaplan, *Biomaterials* 2005, **26**, 5474-5491.
23 T. Peltola, M. Jokinen, H. Rahiala, E. Levänen, J. B. Rosenholm, I. Kangasniemi and A. Yli-Urpo, *J. Biomed. Mater. Res.* 1999, **44**,12-21.
24 A. Tampieri, M. Iafisco, M. Sandri, S. Panseri, C. Cunha, S. Sprio, E. Savini, M. Uhlarz and T. Herrmannsdörfer, *ACS Appl. Mater. Interfaces* 2014, **6**, 15697-15707.
25 K. Lin, P. Liu, L. Wei, Z. Zou, W. Zhang, Y. Qian, Y. Shen and J. Chang, *Chem. Eng. J.* 2013, **222**, 49-59.
26 Z. Q. Su, J. F. Li, Z. F. Ouyang, M. M. L. Arras, G. Wei and K. D. Jandt, *RSC Adv.* 2014, **4**, 14833-14839.
27 J. Zhao, W. Han, M. Tu, S. Huan, R. Zeng, H. Wu, Z. Cha and C. Zhou, *Mater. Sci. Eng. C* **2012**, *32*, 1496-1502.
28 A. Koc, G. Finkenzeller, A. E. Elcin, G. B. Stark and Y. M. Elcin, *J. Biomater. Appl.* **2014**, *29*, 748-760.
29 J. Yang, T. Long, N. F. He, Y. P. Guo, Z. A. Zhu and Q. F. Ke, *J. Mater. Chem. B* 2014, **2**, 6611-6618.
30 Y. Huang, X. Jin, X. Zhang, H. Sun, J. Tu, T. Tang, J. Chang and K. Dai, *Biomaterials* 2009, **30**, 5041-5048.
31 L. Zheng, F. Yang, H. Shen, X. Hu, C. Mochizuki, M. Sato, S. Wang and Y. Zhang, *Biomaterials* 2011, **32**, 7053-7059.
32 C. A. Gregory, W. G. Gunn, A. Peister and D. J. Prockop, *Anal. Biochem.* 2004, **329**, 77-84.
33 P. P. Spicer, J. D. Kretlow, S. Young, J. A. Jansen, F. K. Kasper and A. G. Mikos, *Nat. Protoc.* 2012, **7**, 1918-1929.
34 Y. Deng, H. Zhou, D. Zou, Q. Xie, X. Bi, P. Gu and X. Fan, *Biomaterials* 2013, **34**, 6717-6728.
35 L. Tortet, J. R. Gavarri and G. Nihoul, *J. Solid State Chem.*1997, **132**, 6-16.
36 H. A. Lowenstam and S. Weiner, Oxford University Press, NY, 1989.
37 R. A. Robinson and M. L. Watson, *Anat. Rec.* 1952, **114**, 383-409.
38 S. A. Jackson, A. G. Cartwright and D. Lewis, *Calcif. Tissue Res.*, 1978, **25**, 217-222.
39 G. Lawrie, I. Keen, B. Drew, L. Rintoul, P. Fredericks and L. Grondahl, *Biomacromolecules* 2007, **8**, 2533-2541.
40 B. Li, Y. Wang, D. Jia, Y. Zhou and W. Cai, *Biomed. Mater.* 2009, **4**, 015011.
41 I. Corazzari, R. Nisticò, F. Turci, M. G. Faga, F. Franzoso, S. Tabasso and G. Magnacca, *Polym. Degrad. Stabil.* 2015, **112**, 1-9.
42 D. Tadic and M. Epple, *Biomaterials* 2004, **25**, 987-994.
43 C. B. Baddiel and E. E. Berry, *Spectrochim. Acta* 1966, **22**, 1407-1416.
44 D. Walsh, T. Furuzono and J. Tanaka, *Biomaterials* 2001, **22**, 1205-1212.
45 X. Lu and Y. Leng, *Biomaterials* 2005, **26**, 1097-1108.
46 V. Ottani, D. Martini, M. Franchi, A. Ruggeri and M. Raspanti, *Micron* 2002, **33**, 587-596.
47 J. Wang and C. Liu, *J. Bionic Eng.* 2014, **11**, 600-609.
48 K. Rezwan, Q. Z. Chen, J. J. Blaker and A. R. Boccaccini, *Biomaterials* 2006, **27**, 3413-3431.
49 D. F. Williams, *Biomaterials* 2008, **29**, 2941-2953.
50 J. M. Seong, B. C. Kim, J. H. Park, I. K. Kwon, A. Mantalaris and Y. S. Hwang, *Biomed. Mater.* 2010, **5**, 062001.
51 E. Gomez-Barrena, P. Rosset, I. Muller, R. Giordano, C. Bunu, P. Layrolle, Y. T. Konttinen and F. P. Luyten, *J. Cell Mol. Med.* 2011, **15**,1266-1286.
52 E. Kon, A. Muraglia, A. Corsi, P. Bianco, M. Marcacci, I. Martin, A. Boyde, I. Ruspantini, P. Chistolini, M. Rocca, R. Giardino, R. Cancedda and R. Quarto, *J. Biomed. Mater. Res.* 2000, **49**, 328-337.
53 F. P. Barry and J. M. Murphy, *Int. J. Biochem. Cell Biol.* 2004, **36**, 568-584.
54 Y. W. Wang, Q. Wu and G. Q. Chen, *Biomaterials* **2004**, *25*, 669-675.
55 Q. Liu, L. Cen, S. Yin, L. Chen, G. Liu, J. Chang and L. Cui, *Biomaterials* 2008, **29**, 4792-4799.
56 L. Meinel, S. Hofmann, O. Betz, R. Fajardo, H. P. Merkle, R. Langer, C. H. Evans, G. Vunjak-Novakovic and D. L. Kaplan, *Biomaterials* 2006, **27**, 4993-5002.
57 A. J. Engler, S. Sen, H. L. Sweeney and D. E. Discher, *Cell* 2006, **126**, 677-689.
58 J. C. Reichert, S. Saifzadeh, M. E. Wullschleger, D. R. Epari, M. A. Schütz, G. N. Duda, H. Schell, M. van Griensven, H. Redl and D. W. Hutmacher, *Biomaterials* 2009, **30**, 2149-2163.
59 E. Marin, M. I. Briceno and C. Caballero-George, *Int. J. Nanomed.* 2013, **8**, 3071-3091.
60 W. Graisuwan, O. Wiarachai, C. Ananthanawat, S. Puthong, S. Soogarun, S. Kiatkamjornwong and V. P. Hoven, *J. Colloid Interf. Sci.* 2012, **376**, 177-188.

61 G. C. Wang, L. Zheng, H. S. Zhao, J. Y. Miao, C. H. Sun, H. Liu, Z. Huang, X. Q. Yu, J. Y. Wang and X. T. Tao, *ACS Appl. Mater. Inter.* 2011, **3**, 1692-1701.

Graphical Abstract
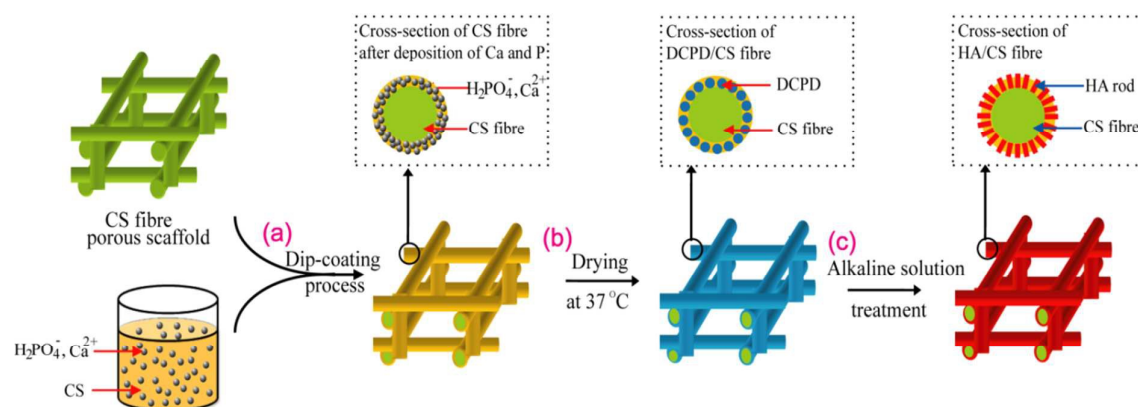
A bioinspired strategy has been developed to fabricate hybrid nanostructured hydroxyapatite/chitosan composite scaffold for bone tissue engineering.